

Paramagnetic Solids

How to cite:

International Edition: doi.org/10.1002/anie.202102740

German Edition: doi.org/10.1002/ange.202102740

Unravelling the Fast Alkali-Ion Dynamics in Paramagnetic Battery Materials Combined with NMR and Deep-Potential Molecular Dynamics Simulation

 Min Lin⁺, Xiangsi Liu⁺, Yuxuan Xiang, Feng Wang, Yunpei Liu, Riqiang Fu, Jun Cheng,^{*} and Yong Yang^{*}

Abstract: Solid-state nuclear magnetic resonance (ssNMR) has received extensive attention in characterizing alkali-ion battery materials because it is highly sensitive for probing the local environment and dynamic information of atoms/ions. However, precise spectral assignment cannot be carried out by conventional DFT for high-rate battery materials at room temperature. Herein, combining DFT calculation of paramagnetic shift and deep potential molecular dynamics (DPMD) simulation to achieve the converged Na⁺ distribution at hundreds of nanoseconds, we obtain the statistically averaged paramagnetic shift, which is in excellent agreement with ssNMR measurements. Two ²³Na shifts induced by different stacking sequences of transition metal layers are revealed in the fast chemically exchanged NMR spectra of P2-type Na_{2/3}(Mg_{1/3}Mn_{2/3})O₂ for the first time. This DPMD simulation auxiliary protocol can be beneficial to a wide range of ssNMR analysis in fast chemically exchanged material systems.

Introduction

Modern fast-paced lifestyle requires the superior fast-charging/discharging performance in the portable devices, electric vehicles and smart-grids.^[1,2] The P2-type layered structure (ABBA-stacking),^[3] which mostly appears in sodium oxides material, is well known as its two-dimensional diffusion channel and excellent ionic conductivity, thus pointing a fertile development path of cost-effective sodium-ion batteries (SIBs) in fast-charging/discharging scenario.^[4] Note that the power density of P2-type Na_{2/3}MnO₂ can be further improved by Mg²⁺ doping in transition metal (TM)

layers^[5] and the highly reversible oxygen reaction can be effectively triggered to provide additional capacity when the fractions of Mg²⁺ reaches 1/3.^[6] Therefore, P2-type Na_{2/3}(Mg_{1/3}Mn_{2/3})O₂ material has attracted widespread attention,^[6–9] and revealing its fine structure and the fast dynamics of alkali-ion is of the central importance.

Solid-state (ss) magic angle spinning (MAS) NMR spectroscopy is a unique tool for characterizing those paramagnetic solids as it is sensitive to local environments.^[10] Nevertheless, associating the local environments with experimental paramagnetic shifts requires the first-principles representations of complex interaction between unpaired TM d-electrons and observed nucleus.^[11] In the past decade, the density functional theory (DFT) methodology has been continuously developed for calculating paramagnetic shift,^[12–15] and it seems to be able to assign the chemical shift in experimental NMR spectrum to each local structure of materials. However, the application of state-of-art DFT methodology is still limited in sluggish alkali-ion dynamic system, such as polyanion,^[12,15–19] full lithiated layered^[18,20,21] and spinel^[22] materials, in which the computational shift has one-to-one correspondence with experimental shift based on the DFT optimized structure (i.e. 0 K) (Figure 1 a). For the promising high-rate battery materials, such as aforesaid P2-type layered materials, the Na⁺ hops frequently between different chemical sites during NMR experiment time,^[23] namely fast chemical exchange regime (Figure 1 b), resulting in the averaged shift across multiple sites and hiding many structural information in previous ²³Na NMR experimental studies.^[24–32] It is worth noting that fast chemical exchange is a general phenomenon in ssNMR studies of high-rate battery materials. For example, Grey's group reported that the fractions of Li⁺ in fast and slow chemical exchange regime could be regarded as a descriptor for measuring Li⁺ dynamics in de-lithiated Li(Ni_{1–x–y}Co_xMn_y)O₂ at different state of charge.^[33] Therefore, the suitable calculation method is urgently needed to further disclose both structural and dynamics information in fast chemically exchanged ssNMR spectra of high-rate battery materials.



Molecular dynamics (MD) simulation is a manifest solution for incorporating chemical exchange in NMR spectra. Although DFTMD calculation can yield accurate diffusion trajectories, it is usually limited in picosecond (ps) timescale due to its high computational cost. As a result, insufficient sampling of alkali-ion hopping and distribution hinder the linking to chemically exchanged NMR spectra. We note that the recently developed deep potential molecular dynamic

[*] M. Lin,^[†] X. Liu,^[†] Y. Xiang, F. Wang, Y. Liu, J. Cheng, Y. Yang
 Collaborative Innovation Center of Chemistry for Energy Materials
 State Key Laboratory for Physical Chemistry of Solid Surface
 College of Chemistry and Chemical Engineering
 Xiamen University, Xiamen 361005 (China)
 E-mail: chengjun@xmu.edu.cn
 yyang@xmu.edu.cn

Y. Yang
 College of Energy, Xiamen University, Xiamen 361005 (China)

R. Fu
 National High Magnetic Field Laboratory
 1800 E. Paul Dirac Drive, Tallahassee, FL 32310 (USA)

[†] These authors contributed equally to this work.

 Supporting information and the ORCID identification number(s) for the author(s) of this article can be found under:
 <https://doi.org/10.1002/anie.202102740>.

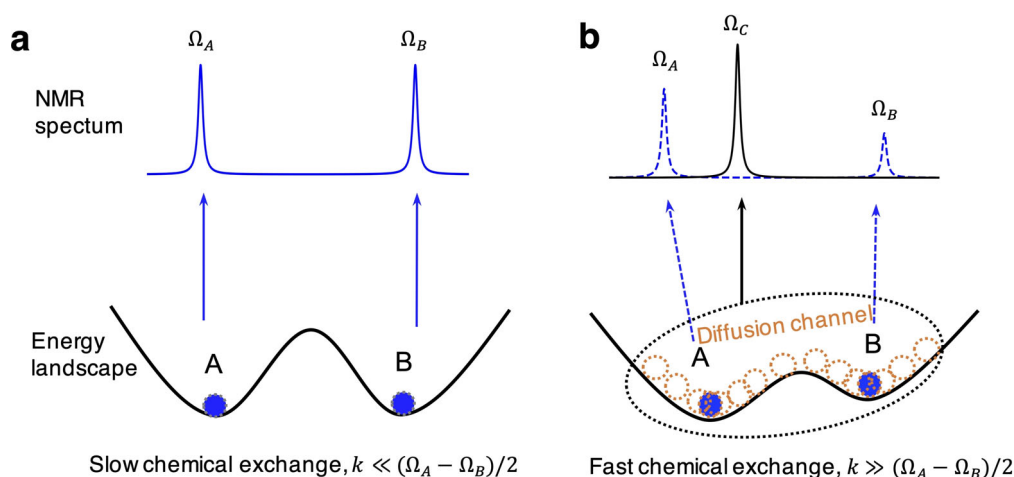


Figure 1. Diagram of slow (a) and fast (b) NMR chemical exchange regimes. k and Ω is the hopping/exchange rate and chemical shift (hertz unit), respectively.

(DPMD) simulation scheme can be a highly computational efficient and accurate solution,^[34] in which atomic coordinates are translated into symmetry conservation descriptors that enable DFT datasets to be trained in deep neural networks (NNs) (Figure 2). The well-trained DP model can massively accelerate MD sampling millions of times faster than DFTMD, which is appropriate for revealing the fast alkali-ion dynamics in paramagnetic battery materials when combining with DFT calculation of chemical shift and NMR experiment.

In this work, P2-type $\text{Na}_{2/3}(\text{Mg}_{1/3}\text{Mn}_{2/3})\text{O}_2$ ^[6,7] is selected as a model system to expand the scope of ssNMR applications to high-rate battery materials. The ^{23}Na paramagnetic shifts at

distinct chemical sites are firstly calculated using DFT method and then the chemically exchanged shift at room temperature is further obtained with the aid of DPMD simulations.^[34] Based on this new scheme, the isotropic shifts in the ^{23}Na spectrum are assigned to the two mixed stacking sequences of TM layers, the space group $P6_3/mcm$ and $P6_322$, and further are accurately quantified. Our results not only correct the structural assignment of P2-type $\text{Na}_{2/3}(\text{Mg}_{1/3}\text{Mn}_{2/3})\text{O}_2$ to single phase ($P6_3/mcm$) in previous reports,^[7,9] but also offer an effective approach to unravel the fast chemically exchanged ssNMR spectra of high-rate battery materials.

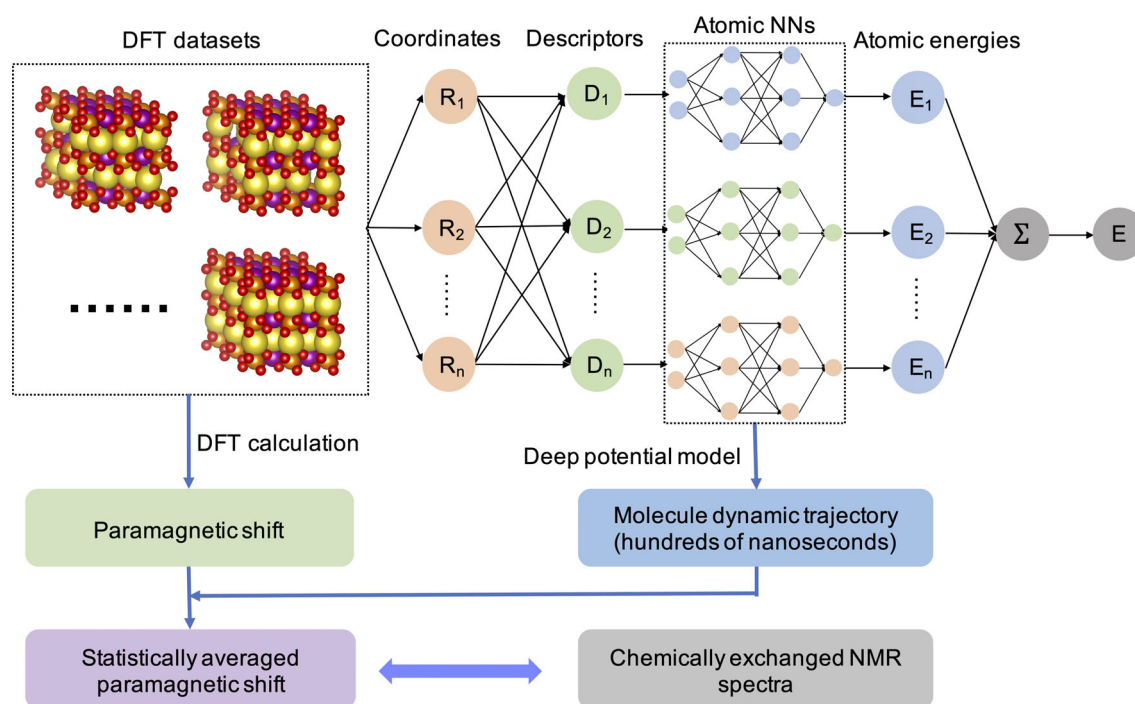


Figure 2. Flowchart of computing statistically averaged paramagnetic shifts.



Results and Discussion

$P2\text{-Na}_{2/3}(\text{Mg}_{1/3}\text{Mn}_{2/3})\text{O}_2$ is normally regarded as a single phase with the space group of $P6_3/mcm$ in previous works.^[7,9] The TM layers containing $\text{Mg}^{2+}/\text{Mn}^{4+}$ honeycomb ordering stack along z axis facing the same metal element on neighboring TM layers, which induces three distinct Na^+ sites, that is, edge (Na_{edge}), Mn-Mn face ($\text{Na}_{\text{Mn-Mn}}$) and Mg-Mg face ($\text{Na}_{\text{Mg-Mg}}$) sites (Figure 3 a,b). Nevertheless, only one isotropic shift is anticipated in the ^{23}Na NMR spectrum because of the superior interlayer Na^+ mobility in P2-type materials,^[25,35] in which the Na^+ hopping rate is over than NMR time resolution limit as mentioned above (Figure 2 b).

^{23}Na MAS variable-offset cumulative spectroscopy (VOCS) were acquired at the temperature of 298 K, 308, 318, and 328 K at 50 kHz spinning rate and 9.4 T (Figure 4 a). As shown in the Supporting Information, Figure S1, the spectra at each temperature is obtained by summing individual spectrum with variable offset frequency. In contrast to our expectation, two ^{23}Na isotropic shifts labeled as Peak1 and Peak2 are observed in the paramagnetic region of ^{23}Na MAS NMR spectra (Figure 4 a), which decrease from 1665 to 1611 ppm and 1522 to 1475 ppm as the temperature increasing from 298 to 328 K, respectively. The number of isotopic shifts has been further confirmed via a MAS NMR experi-

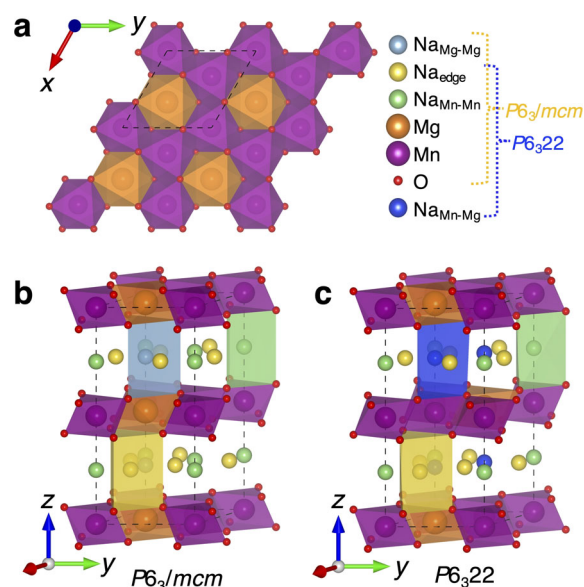


Figure 3. Crystal structures of $P2\text{-Na}_{2/3}(\text{Mg}_{1/3}\text{Mn}_{2/3})\text{O}_2$. a) Top view of the honeycomb ordering of Mg^{2+} and Mn^{4+} in $2 \times 2 \times 1$ supercell. The oblique views of b) $P6_3/mcm$ and c) $P6_322$ unit cell. Only one prism of each distinct site is shown in unit cells for clarification. Note that the number ratio of distinct sites is $\text{Na}_{\text{edge}}:\text{Na}_{\text{Mn-Mn}}:\text{Na}_{\text{Mg-Mg}} = 3:2:1$ in $P6_3/mcm$, and $\text{Na}_{\text{edge}}:\text{Na}_{\text{Mn-Mn}}:\text{Na}_{\text{Mn-Mg}} = 3:1:2$ in $P6_322$.

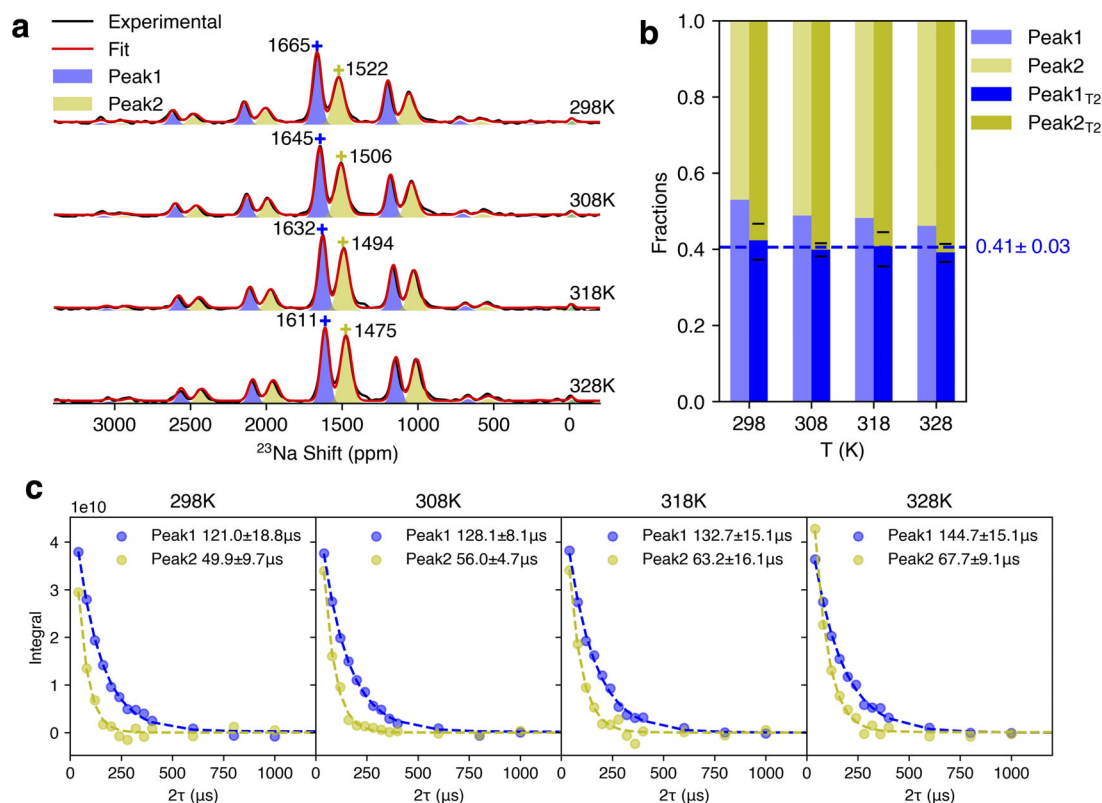


Figure 4. ^{23}Na NMR spectra and T_2 measurement of $P2\text{-Na}_{2/3}(\text{Mg}_{1/3}\text{Mn}_{2/3})\text{O}_2$. a) Variable-temperature ^{23}Na NMR VOCS spectra and fitting curves, in which the peaks of isotropic shifts are labeled with “+” and the intensities of spectra are plotted at absolute scale. b) The quantification of Peak1 and Peak2 analyzed upon the VOCS spectra. The histogram labeled with subscript “T2” stands for the fractions after T_2 calibration. The mean value of calibrated fractions of Peak1 is indicated by the dashed blue line, and error bars at each temperature are labeled using short black lines. c) The transverse relaxation T_2 of Peak1 and Peak2. The integrals and fitting curves are plotted using filled circles and dashed lines, respectively. T_2 values and its standard deviation are shown in the legends.

ment at 60 kHz spinning rate and 14.1 T to suppress the second order quadrupolar line broadening of ^{23}Na NMR spectra (Supporting Information, Figure S2). The negative correlation between the shift and the temperature rising clearly shows the typical characteristic of paramagnetic shift.^[36] In addition, the transverse relaxation time T_2 of Peak1 and Peak2 increases with the temperature rising (Figure 4c), from 121.0 ± 18.8 to 144.7 ± 15.1 μs and 49.9 ± 9.7 to 67.7 ± 9.1 μs , respectively, indicating that both ^{23}Na shifts are located in fast exchange regime.^[37] Besides, the longer T_2 of Peak1 suggests the higher Na^+ mobility in the chemical environment of Peak1 than that of Peak2. Apparently, the single $P6_3/mcm$ cannot be related to two isotropic shifts in ^{23}Na MAS NMR spectra, thus we tentatively propose other P2-type stacking sequence belonging to $P6_322$ space group, in which Mg^{2+} is staggered along z axis in adjacent layers, giving additional Mn-Mg face ($\text{Na}_{\text{Mn-Mg}}$) Na^+ site (Figure 3c). The formation energy of $P6_322$ $2 \times 2 \times 1$ supercell is 0.05 eV/supercell lower than that of $P6_3/mcm$ (Supporting Information, Figure S5), indicating that $P6_322$ is thermodynamically stable. Although the integral of Peak2 obviously increases with elevated temperature, the fractions of Peak2 are quantified as 0.41 ± 0.03 based on VOCS spectra at variable temperatures (Figure 4b) after taking into account the transverse relaxation effects during the echo periods.^[37] Given that no transform between $P6_3/mcm$ and $P6_322$ by interlayer slipping is expected in such a narrow variable temperature range,^[38] two isotropic shifts may correspond to interlayer averaged ^{23}Na shift of $P6_3/mcm$ and $P6_322$, respectively.

The assignment of the ^{23}Na NMR spectrum is assisted with the all-electron hybrid functional DFT calculations of $P6_3/mcm$ and $P6_322$. Three unpaired electrons locate in e_g orbital of octahedral coordinated Mn^{4+} of $\text{P2-Na}_{2/3}(\text{Mg}_{1/3}\text{Mn}_{2/3})\text{O}_2$, and the highly symmetrical occupation of 3d electrons usually leads to small pseudocontact shift and neglectable zero-field splitting (ZFS) effect.^[15,39] In other words, paramagnetic shift is dominated by Fermi contact shift (δ_{FC}),^[18] which originates from the spin-transfer through Mn-O-Na pathway from octahedrally coordinated Mn^{4+} 3d- e_g orbital to Na 1s orbital. Second order quadrupole shift^[40] (δ_{OIS}) is also included in total computational shift (δ_{cal}). Given that δ_{FC} strongly depends on the content (α) of Hatree-Fock exchange mixed in hybrid functional,^[12,16] $\alpha = 0.20, 0.25$ and 0.30 are used individually and the detailed results are shown in the Supporting Information, Table S1. When $\alpha = 0.25$, the ^{23}Na shift of Na_{edge} , $\text{Na}_{\text{Mn-Mn}}$ and $\text{Na}_{\text{Mg-Mg}}$ sites are 2402–2587, 19 and 2216 ppm, respectively (Figure 5a). Note that, $\text{Na}_{\text{Mn-Mg}}$ can be regarded as a combination of half of $\text{Na}_{\text{Mn-Mn}}$ and $\text{Na}_{\text{Mg-Mg}}$, thus the additivity of δ_{FC} ^[18] also verified by the fact that the shift of $\text{Na}_{\text{Mn-Mg}}$ site (1191 ppm) approximates to the mid-point shift of $\text{Na}_{\text{Mn-Mn}}$ and $\text{Na}_{\text{Mg-Mg}}$ sites (1117.5 ppm). The experimental shifts locate in the broad range of δ_{cal} of distinct sites, 19–2587 ppm, which is consistent with the averaged shift across distinct sites.

Owing to the rapid Na^+ hopping, the above calculated chemical shift for each Na^+ site cannot correspond to the experimental shift. The further computing of the layer averaged ^{23}Na shift requires distribution probabilities of

Na^+ at distinct sites. We adopt the recently developed deep potential molecular dynamics (DPMD)^[34] method, utilizing many-body potential and interatomic forces generated by deep neural networks trained with ab initio datasets. The DP model can dramatically extend the MD simulation timescale, 1.5 ns MD simulation can be obtained using a well-trained DP model on a NVIDIA GeForce RTX 2080 Ti GPU card within one hour, which would take around 3 years using DFTMD on one node composed by 28 parallel Intel Xeon E5-2680 v4 CPU cores. We acquire well converged Na^+ distribution at 300 K after 200 ns MD simulation (Supporting Information, Figure S10a,b), and the distribution probabilities are 0.586, 0.411, 0.003 for Na_{edge} , $\text{Na}_{\text{Mn-Mn}}$, $\text{Na}_{\text{Mg-Mg}}$ of $P6_3/mcm$ and 0.656, 0.242, 0.102 for Na_{edge} , $\text{Na}_{\text{Mn-Mn}}$, $\text{Na}_{\text{Mn-Mg}}$ of $P6_322$, respectively (Figure 5b,c). Although the Na^+ distribution converges in a short simulation time at higher temperatures and the simulation time can be shortened to several nanoseconds at 500 K, the higher temperature also results in remarkably Na^+ redistribution (Supporting Information, Figure S10c–f). Therefore, the high temperature enhanced sampling usually employed in DFTMD^[41] is not appropriate for computing Na^+ distribution at room temperature, thus further highlighting the importance of DPMD. According to Na^+ distribution results from DPMD at 300 K, the averaged shifts are 1474 ppm for $P6_3/mcm$ and 1762 ppm for $P6_322$ when $\alpha = 0.25$ (Figure 5a). Consequently, Peak1 (1665 ppm) and Peak2 (1522 ppm) can be assigned to interlayer averaged signal of ^{23}Na in $P6_322$ and $P6_3/mcm$ in $\text{Na}_{2/3}(\text{Mg}_{1/3}\text{Mn}_{2/3})\text{O}_2$, respectively. Moreover, Na^+ distribution map (Figure 5b,c) suggests a honeycomb Na^+ diffusion channel connected by face and edge sites in both phases. The more uniform Na^+ distribution in $P6_322$ indicates a smoother potential energy surface, which contributes to the difference of the averaged shifts between two stacking sequences. Furthermore, based on the linear fitting of Na^+ mean-squared displacement (MSD), Na^+ diffusion coefficients (D_{Na}) are estimated to be 1.3×10^{-7} and 4.4×10^{-7} cm^2s^{-1} for $P6_3/mcm$ and $P6_322$ at 300 K, respectively. Thousands of \AA^2 Na^+ MSD after 200 ns simulations (Figure 5d,e) reduce relative standard deviation (RSD) of D_{Na} to about 10%.^[41] The higher Na^+ mobility in $P6_322$ is also consistent with longer T_2 of Peak1 ($P6_322$) due to faster Na^+ diffusion in fast exchange regime.

Discussion

To further confirm above assignments, the powder X-ray diffraction (PXRD) pattern simulations and the refinement of $\text{P2-Na}_{2/3}(\text{Mg}_{1/3}\text{Mn}_{2/3})\text{O}_2$ are performed by using fully random stacking models of $P6_3/mcm$ and $P6_322$ (Supporting Information, Figure S11a). The refinement results (Supporting Information, Figure S12a) suggest that 39% of $P6_322$ exists in $\text{P2-Na}_{2/3}(\text{Mg}_{1/3}\text{Mn}_{2/3})\text{O}_2$, which is in excellent agreement with the analysis of ^{23}Na NMR spectrum ($41 \pm 3\%$), the detailed results and discussions are presented in the Supporting Information, Figure S12. More importantly, the new assignment enables ssNMR accurately quantifying the fractions of different stacking in similar honeycomb-ordered cathode materials, since the peak integral of NMR spectra indicates



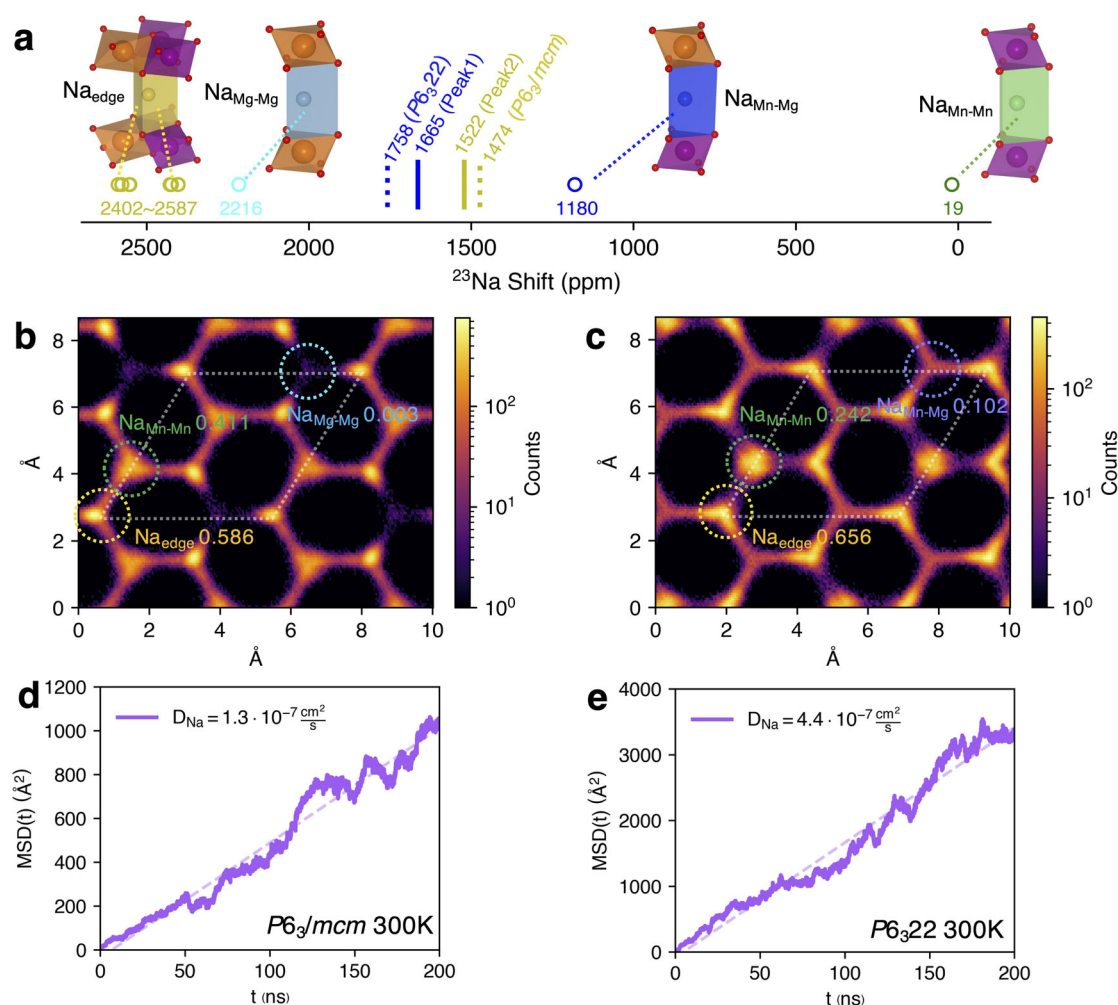


Figure 5. Calculation of ^{23}Na chemical shifts, Na^+ distribution and diffusion. a) Computational ^{23}Na chemical shift (298 K) and Na^+ local environments. Experimental shifts and computational averaged shifts are labeled with solid and dashed vertical lines, respectively. The distribution map of Na^+ on XY plane based on 200 ns DPMD simulations at 300 K for both b) $\text{P6}_3/mcm$ and c) P6_322 . The analysis of distribution probability uses site centered cycles with a radius of 0.8 Å as indicated by dashed cycles, and the calculated probabilities are labeled. The dashed rhombus indicates the XY plane of unit cells. The numbers of Na^+ are counted using a time interval of 2 ps and not normalized. MSD(t) and D_{Na} in d) P6_322 and $\text{P6}_3/mcm$ at 300 K with a simulation time of 200 ns. The dashed purple lines indicate the linear fitting of MSD(t) during whole simulation time.

alkali-ion content in different stacking sequence directly, the ^{23}Na NMR spectrum of $\text{P2-Na}_{2/3}(\text{Mg}_{0.28}\text{Mn}_{0.72})\text{O}_2$ is further selected for illustrating this point (Supporting Information, Figure S3). Based on above experimental and computational results, two shifts locating at 1581 ppm and 1457 ppm of $\text{Na}_{2/3}(\text{Mg}_{0.28}\text{Mn}_{0.72})\text{O}_2$ are assigned to P6_322 and $\text{P6}_3/mcm$, respectively. In contrast to $\text{P2-Na}_{2/3}(\text{Mg}_{1/3}\text{Mn}_{2/3})\text{O}_2$, the fraction of P6_322 in NMR spectra is much smaller, suggesting that the stacking sequence is easily adjusted by changing the stoichiometric ratio of Mg and Mn, such that the $\text{P2-Na}_{2/3}(\text{Mg}_{0.28}\text{Mn}_{0.72})\text{O}_2$ is refined as purely $\text{P6}_3/mcm$ in previous work.^[9] Furthermore, a recent DFT study rationalizes the high stability of oxygen redox in $\text{P2-Na}_{2/3}(\text{Mg}_{1/3}\text{Mn}_{2/3})\text{O}_2$ through collective distortion of oxygen network in $\text{P6}_3/mcm$.^[7] According to their conclusion, we anticipate that $\text{P6}_3/mcm$ phase would exhibit the better oxygen redox reversibility during electrochemical reaction, due to its atomic sequence in z direction is composed by symmetric Mn-O-O-

Mn and Mg-O-O-Mg units. For the P6_322 phase, the O-O pair in asymmetric Mn-O-O-Mg unit may result in bias distortion to Mn or Mg, which is harmful for reversible oxygen redox. Anyway, the oxygen redox behavior of P6_322 should be considered carefully in the future experimental and theoretical studies, improving the oxygen redox reversibility of $\text{P2-Na}_{2/3}(\text{Mg}_{1/3}\text{Mn}_{2/3})\text{O}_2$ by tuning the fractions of P6_322 would deserve the future investigations.

Conclusion

Two unexpected isotropic shifts located at 1665 and 1522 ppm are observed experimentally in ^{23}Na MAS NMR spectra of $\text{P2-Na}_{2/3}(\text{Mg}_{1/3}\text{Mn}_{2/3})\text{O}_2$, which can be attributed to Fermi contact interaction and fast chemical exchange of Na^+ between prismatic sites in Na interlayers. The shifts of distinct sites are calculated using all electron DFT methodology with

hybrid functionals, further combining with Na⁺ distribution analyzed from 200 ns DPMD simulations that enable the fast chemically exchanged shifts to be calculated in paramagnetic battery materials for the first time. As a result, the experimental ²³Na shifts of P2-Na_{2/3}(Mg_{1/3}Mn_{2/3})O₂ are assigned to two stacking sequences that correspond to the space group *P6₃/mcm* (1665 ppm) and *P6₃22* (1522 ppm). Furthermore, the NMR deconvoluted intensity gives 41 ± 3 % of *P6₃22*, which is in excellent agreement with PXRD refinement of mixed stacking that gives a probability of 39 % for *P6₃22*. It is anticipated that the combination of ssNMR experiment, chemical shift calculation and DPMD simulation as demonstrated in this work can be applicable for interpreting the NMR spectra of high-rate paramagnetic battery materials and other widely dynamic systems.

Acknowledgements

This work is financially supported by National Key Research and Development Program of China (Grant nos. 2016YFB0901502, 2018YFB0905400), National Natural Science Foundation of China (Grant Nos. 21991151, 21991150, 21935009, 21761132030, 21861132015, 22021001). This work is also funded by the Graduate School of Xiamen University via a visiting scholarship for M.L. M.L. thanks Dr. Jinxiao Mi, Dr. Andrew J. Pell, Dr. Aleksander Jaworski, and Rihards Aleksis for their useful discussion. Dr. Riqiang Fu thanks to the support from the National High Magnetic Field Laboratory, which is supported by NSF Cooperative Agreement DMR-1644779 and the State of Florida.

Conflict of interest

The authors declare no conflict of interest.

Keywords: chemical exchange · deep potential · density functional calculations · NMR spectroscopy · paramagnetic solids

- [1] A. Tomaszewska, Z. Chu, X. Feng, S. O'Kane, X. Liu, J. Chen, C. Ji, E. Endler, R. Li, L. Liu, Y. Li, S. Zheng, S. Vetterlein, M. Gao, J. Du, M. Parkes, M. Ouyang, M. Marinescu, G. Offer, B. Wu, *eTransportation* **2019**, *1*, 100011.
- [2] Y. Liu, Y. Zhu, Y. Cui, *Nat. Energy* **2019**, *4*, 540–550.
- [3] C. Delmas, *Adv. Energy Mater.* **2018**, *8*, 1703137.
- [4] X. Liu, W. Zuo, B. Zheng, Y. Xiang, K. Zhou, Z. Xiao, P. Shan, J. Shi, Q. Li, G. Zhong, R. Fu, Y. Yang, *Angew. Chem. Int. Ed.* **2019**, *58*, 18086–18095; *Angew. Chem.* **2019**, *131*, 18254–18263.
- [5] R. J. Clément, J. Billaud, A. R. Armstrong, G. Singh, T. Rojo, P. G. Bruce, C. P. Grey, *Energy Environ. Sci.* **2016**, *9*, 3240–3251.
- [6] K. Dai, J. Wu, Z. Zhuo, Q. Li, S. Sallis, J. Mao, G. Ai, C. Sun, Z. Li, W. E. Gent, W. C. Chueh, Y. Chuang, R. Zeng, Z. Shen, F. Pan, S. Yan, L. F. J. Piper, Z. Hussain, G. Liu, W. Yang, *Joule* **2019**, *3*, 518–541.
- [7] J. Vergnet, M. Saubanère, M.-L. Doublet, J.-M. Tarascon, *Joule* **2020**, *4*, 420–434.
- [8] M. Ben Yahia, J. Vergnet, M. Saubanère, M.-L. Doublet, *Nat. Mater.* **2019**, *18*, 496–502.
- [9] U. Maitra, R. A. House, J. W. Somerville, N. Tapia-Ruiz, J. G. Lozano, N. Guerrini, R. Hao, K. Luo, L. Jin, M. A. Pérez-Osorio, F. Massel, D. M. Pickup, S. Ramos, X. Lu, D. E. McNally, A. V. Chadwick, F. Giustino, T. Schmitt, L. C. Duda, M. R. Roberts, P. G. Bruce, *Nat. Chem.* **2018**, *10*, 288–295.
- [10] C. P. Grey, N. Dupré, *Chem. Rev.* **2004**, *104*, 4493–4512.
- [11] D. Carlier, M. Ménétrier, C. P. Grey, C. Delmas, G. Ceder, *Phys. Rev. B* **2003**, *67*, 174103.
- [12] J. Kim, D. S. Middlemiss, N. A. Chernova, B. Y. X. Zhu, C. Masquelier, C. P. Grey, *J. Am. Chem. Soc.* **2010**, *132*, 16825–16840.
- [13] R. Pigliapochi, A. J. Pell, I. D. Seymour, C. P. Grey, D. Ceresoli, M. Kaupp, *Phys. Rev. B* **2017**, *95*, 054412.
- [14] A. Mondal, M. W. Gaultois, A. J. Pell, M. Iannuzzi, C. P. Grey, J. Hutter, M. Kaupp, *J. Chem. Theory Comput.* **2018**, *14*, 377–394.
- [15] A. Mondal, M. Kaupp, *J. Phys. Chem. Lett.* **2018**, *9*, 1480–1484.
- [16] Y. Zhang, A. Castets, D. Carlier, M. Ménétrier, F. Boucher, *J. Phys. Chem. C* **2012**, *116*, 17393–17402.
- [17] R. J. Clément, A. J. Pell, D. S. Middlemiss, F. C. Strobridge, J. K. Miller, M. S. Whittingham, L. Emsley, C. P. Grey, G. Pintacuda, *J. Am. Chem. Soc.* **2012**, *134*, 17178–17185.
- [18] D. S. Middlemiss, A. J. Ilott, R. J. Clément, F. C. Strobridge, C. P. Grey, *Chem. Mater.* **2013**, *25*, 1723–1734.
- [19] Q. Li, Z. Liu, F. Zheng, R. Liu, J. Lee, G.-L. Xu, G. Zhong, X. Hou, R. Fu, Z. Chen, K. Amine, J. Mi, S. Wu, C. P. Grey, Y. Yang, *Angew. Chem. Int. Ed.* **2018**, *57*, 11918–11923; *Angew. Chem.* **2018**, *130*, 12094–12099.
- [20] I. D. Seymour, D. S. Middlemiss, D. M. Halat, N. M. Trease, A. J. Pell, C. P. Grey, *J. Am. Chem. Soc.* **2016**, *138*, 9405–9408.
- [21] P. J. Reeves, I. D. Seymour, K. J. Griffith, C. P. Grey, *Chem. Mater.* **2019**, *31*, 2814–2821.
- [22] R. Pigliapochi, I. D. Seymour, C. Merlet, A. J. Pell, D. T. Murphy, S. Schmid, C. P. Grey, *Chem. Mater.* **2018**, *30*, 817–829.
- [23] M. H. Levitt, *Spin Dynamics: Basics of Nuclear Magnetic Resonance*, 2nd ed, John Wiley & Sons Ltd, Hoboken, **2008**, p.522.
- [24] M. Kalapsazova, S. Ivanova, R. Kukeva, S. Simova, S. Wegner, E. Zhecheva, R. Stoyanova, *Phys. Chem. Chem. Phys.* **2017**, *19*, 27065–27073.
- [25] R. J. Clément, J. Xu, D. S. Middlemiss, J. Alvarado, C. Ma, Y. S. Meng, C. P. Grey, *J. Mater. Chem. A* **2017**, *5*, 4129–4143.
- [26] G. Singh, N. Tapia-Ruiz, J. M. Lopez Del Amo, U. Maitra, J. W. Somerville, A. R. Armstrong, J. Martinez De Ilarduya, T. Rojo, P. G. Bruce, *Chem. Mater.* **2016**, *28*, 5087–5094.
- [27] X. Wu, G. L. Xu, G. Zhong, Z. Gong, M. J. McDonald, S. Zheng, R. Fu, Z. Chen, K. Amine, Y. Yang, *ACS Appl. Mater. Interfaces* **2016**, *8*, 22227–22237.
- [28] J. Hou, J. Song, Y. Niu, C. Cheng, H. He, Y. Li, M. Xu, *J. Solid State Electrochem.* **2015**, *19*, 1827–1831.
- [29] G. Singh, J. M. López Del Amo, M. Galceran, S. Pérez-Villar, T. Rojo, *J. Mater. Chem. A* **2015**, *3*, 6954–6961.
- [30] J. Ma, S. H. Bo, L. Wu, Y. Zhu, C. P. Grey, P. G. Khalifah, *Chem. Mater.* **2015**, *27*, 2387–2399.
- [31] E. Gonzalo, M. H. Han, J. M. López Del Amo, B. Acebedo, M. Casas-Cabanas, T. Rojo, *J. Mater. Chem. A* **2014**, *2*, 18523–18530.
- [32] J. Cabana, N. A. Chernova, J. Xiao, M. Roppolo, K. A. Aldi, M. S. Whittingham, C. P. Grey, *Inorg. Chem.* **2013**, *52*, 8540–8550.
- [33] K. Märker, P. J. Reeves, C. Xu, K. J. Griffith, C. P. Grey, *Chem. Mater.* **2019**, *31*, 2545–2554.
- [34] L. Zhang, J. Han, H. Wang, R. Car, W. E, *Phys. Rev. Lett.* **2018**, *120*, 143001.
- [35] P. Wang, H. Yao, X. Liu, Y. Yin, J. Zhang, Y. Wen, X. Yu, L. Gu, Y. Guo, *Sci. Adv.* **2018**, *4*, eaar6018.
- [36] A. J. Pell, G. Pintacuda, C. P. Grey, *Prog. Nucl. Magn. Reson. Spectrosc.* **2019**, *111*, 1–271.



- [37] L. Zhou, M. Leskes, T. Liu, C. P. Grey, *Angew. Chem. Int. Ed.* **2015**, *54*, 14782–14786; *Angew. Chem.* **2015**, *127*, 14995–14999.
- [38] X. Li, F. Bianchini, J. Wind, P. Vajeeston, D. Wragg, H. Fjellvåg, *J. Electrochem. Soc.* **2019**, *166*, A3830–A3837.
- [39] A. Mondal, M. Kaupp, *J. Phys. Chem. C* **2019**, *123*, 8387–8405.
- [40] A. Jerschow, *Prog. Nucl. Magn. Reson. Spectrosc.* **2005**, *46*, 63–78.
- [41] X. He, Y. Zhu, A. Epstein, Y. Mo, *npj Comput. Mater.* **2018**, *4*, 18.

Manuscript received: February 23, 2021

Accepted manuscript online: March 16, 2021

Version of record online: ■ ■ ■ ■ ■ ■ ■ ■ ■ ■



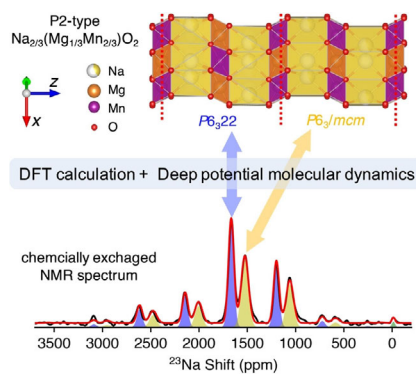
Research Articles



Paramagnetic Solids

M. Lin, X. Liu, Y. Xiang, F. Wang, Y. Liu,
R. Fu, J. Cheng,* Y. Yang* — ■■■■—■■■■

Unravelling the Fast Alkali-Ion Dynamics
in Paramagnetic Battery Materials
Combined with NMR and Deep-Potential
Molecular Dynamics Simulation



The unambiguous assignment of chemical shift in paramagnetic battery materials relies on first-principles calculation, while the state-of-art computational methodology is limited in sluggish dynamic systems. We incorporate hundreds of nanoseconds deep potential molecular dynamics (DPMD) simulation to expanding the ssNMR application in high-rate cathode materials.